JOURNAL OF MATERIALS SCIENCE 32 (1997) 2501–2507

Transmission electron microscopic characterization of zirconia reinforced with silicon carbide fibres

Y. G. WANG
Department of Physics, Norwegian University of Science and Technology, N-7034 Trondheim, Norway

D. H. PING, D. X. LI, J. S. ZHANG
Laboratory of Atomic Imaging of Solids, Institute of Metal Research, Chinese Academy of Sciences, Shenyang 110015, People's Republic of China

R. HØIER
SINTEF Applied Physics, N-7034 Trondheim, Norway

The microstructures of zirconia reinforced with silicon carbide fibres prepared by the sol–gel process have been examined using a transmission electron microscope. The characteristic feature of highly oriented grains of monoclinic zirconia, with its unique *b*-axis as well as *c*-axis of the tetragonal structure nearly all parallel to the hot pressing plane, shows the formation of matrix texture. Twinning in the monoclinic phase was well developed and highly dominated by twinning with the (100) plane as the interface. Alternative twinning with the interfaces parallel to the (001) plane has also been revealed and a possible model was suggested based upon the basic structure to be coincident with the [100] rotation twinning. Strong intergrowth of the tetragonal and monoclinic phases was frequently found and the orientation relationship was determined. The possible orientation variants resulting from the tetragonal to monoclinic phase transformation were proposed based upon such orientations of the lattices. Two of them with the misorientation angle of 9°15′ and 80°45′, respectively, were also found to coexist with the two kinds of twinning. Such texture configuration may have a close relation to the improvement of toughness.

1. Introduction

Zirconia (ZrO_2) has high scientific and technological interest owing to its high melting point ($\sim 2700\,^{\circ}C$), good chemical stability and resistance to corrosion. Extensive studies have been performed to determine the microstructure and toughening response. In fact, advances in the development of ceramics and ceramic composites rely on a detailed understanding of the mechanisms which contribute to the formation of the desired microstructural features necessary to control the mechanical response of the materials. Several studies on the toughening behaviour in zirconia-based ceramics have been reported [1–6]. The results showed that the toughness of zirconia ceramics has a very close relation with the tetragonal–monoclinic phase transformation, i.e. so-called transformation toughening. The increased crack-resistance behaviour is caused by a crack-shielding effect due to the stress-induced tetragonal to monoclinic transformation around the crack tip. This phase transformation has been used as an additional toughening mechanism to improve the mechanical properties of ceramic composites. The fracture strength and fracture toughness of Al_2O_3–SiC–ZrO_2 ceramic have been increased up to 1750 MPa and 6 $MPa\,m^{1/2}$, respectively [7]. In addition, ferroelastic switching, resulting from the monoclinic to tetragonal transformation, has also been considered as a toughening mechanism in zirconia ceramics. The ferroelastic domains giving rise to texture due to crack reflection contribute to higher toughness [8, 9]. The toughness for large-size grains (50–150 μm) in displacively formed t′-zirconia (ferroelastic toughened) is similar to that of monoclinic zirconia with submicrometre grains (transformation toughened) [10].

In order to develop new structural features and to improve the toughening response, it is necessary to adjust the whisker–powder mixing process. Thus, the sol–gel method was used in the present studies for the manufacturing of zirconium oxide ceramics reinforced with silicon carbide fibres. Results from the characterization of the microstructure consisting of various twinning, orientation variants and the well-developed matrix texture, are discussed.

2. Experimental procedure

The sol–gel process was applied to produce silicon carbide fibre-reinforced zirconia ceramic for the purpose of adjusting the technological conditions of the

0022–2461

manufacturing process [11, 12], in order to improve the disadvantages of the fibre–powder mixing process and to develop a new structural feature. The ZrO_2 was prepared from $ZrOCl_2 \cdot 8HO_2$ and Y_2O_3 from aqueous YCl_3 solution. The content of YO_2 in the final product is in the range 3–5 mol %. The β-SiC fibre with length of 20–200 μm, diameter 0.1–2.0 μm, and average tensile strength of 7500 MPa, was produced by the Institute of Metal Research, Chinese Academy of Sciences. SiC whisker mixing in the starting materials $ZrOCl_2 \cdot 8HO_2$ and YCl_3 solution were performed using supersonic vibration (about 15 min) in order to disperse the fibres as uniformly as possibly. The ceramic composite was synthesized by ammonia titration, pH regulation, filtration, drying and followed by sintering (1200 °C) and hot pressing (1600 °C, 34 MPa, 20 min). The details of the procedure were described elsewhere [13].

X-ray diffraction showed the presence of tetragonal ($a = 0.364$, $c = 0.527$ nm and space group $P4_2/nmc$) and monoclinic ($a = 0.517$, $b = 0.523$, $c = 0.534$ nm, $\beta = 99°15'$ and space group $P2_1/c$) phases [14, 15]. The flexural strength was measured by three-point bending with a 25 mm span using 4 mm × 3 mm × 30 mm bars. The indentation test was used to determine the fracture toughness. Cross-section specimens were made for characterization of the microstructure. The thin pieces, about 3 mm diameter and 0.1 mm thick, were cut perpendicular to the hot pressing plane and first mechanically ground down to 50 μm and subsequently dimpled to about 20 μm and finally thinned by ion-beam milling (Gatan, model 600) with argon at the incident angle of 15°. A relatively low voltage (~3 kV) and low current (~10 μA) were used to produce electron-transparent areas. A Philips CM30 transmission electron microscope was used at 300 kV to examine the microstructure in order to understand the dependence of the microstructure on the processing. The objective was to establish processing–structure–properties relations.

3. Results and discussion

3.1. Twinning in monoclinic zirconia

Fig. 1 shows a typical microstructure. It can be seen that the silicon carbide whiskers are all regularly arranged with their growth axis parallel to the hot-pressing plane and dispersed uniformly. Random distribution of whiskers was not observed in this study. Reaction products at the interface between the zirconium oxide and silicon carbide fibres was not found. Electron diffraction microanalysis shows that the transformation of tetragonal to monoclinic zirconium dioxide has widely taken place. Fig. 2 is an electron diffraction pattern with the incident beam parallel to the [0 1 0] zone axis of the monoclinic phase showing twinning with the (1 0 0) plane as interface. Complex multiple twinning in the monoclinic phase is very common and the (1 0 0) twinning is dominant. In addition to the previously reported twinning on the (1 0 0) plane, twinning on the (0 0 1) plane was also detected in this investigation, although more infrequently. Fig. 3 is an electron diffraction pattern from

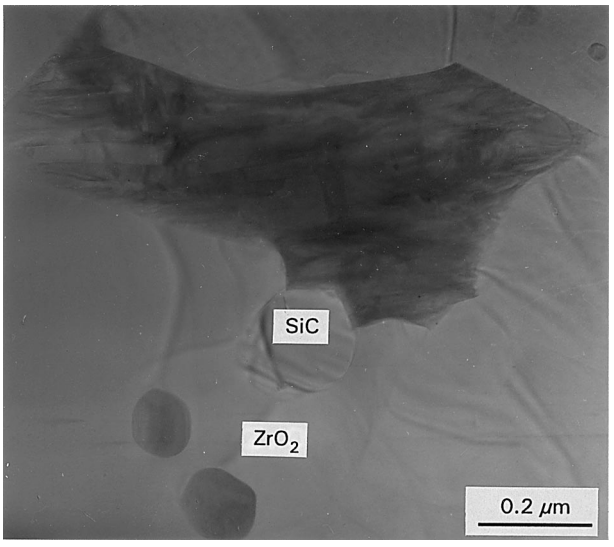

Figure 1 Bright-field micrograph perpendicular to the hot-pressing plane showing a typical microstructure of ZrO_2 ceramic reinforced with β-SiC fibres.

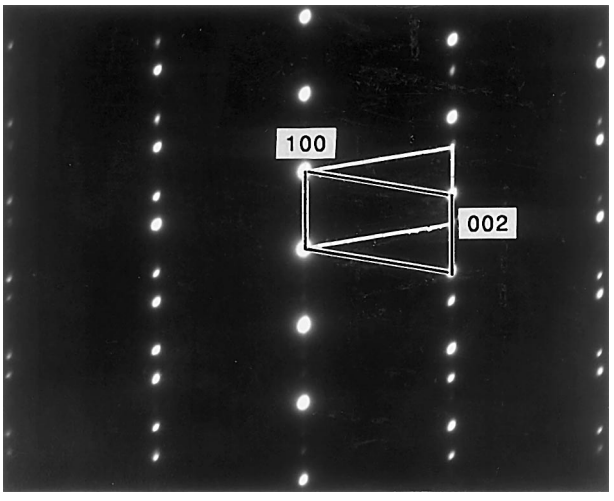

Figure 2 [0 1 0] electron diffraction pattern showing the (1 0 0) twinning in the monoclinic ZrO_2; the repeat units of matrix and twin are outlined by different types of lines.

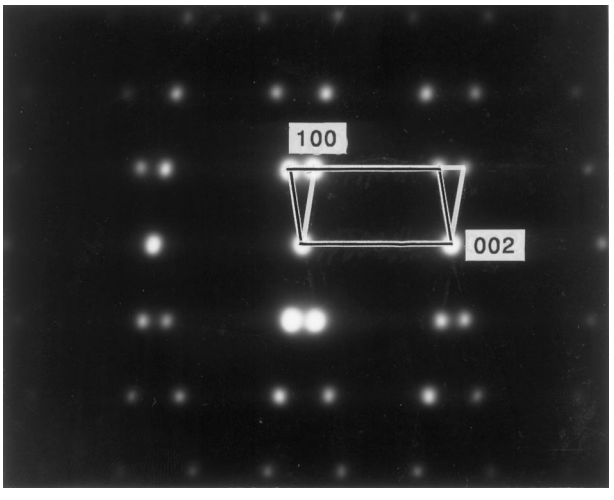

Figure 3 [0 1 0] electron diffraction pattern showing twinning on the (0 0 1) plane of monoclinic ZrO_2.

the monoclinic phase with the incident beam in the same direction as Fig. 2, showing the presence of such twinning. Based on the fundamental structure of the monoclinic zirconia (Fig. 4a), a model of such twinning can be constructed by the operation of a 180° rotation parallel to the [1 0 0] direction through the oxygen atom at the height of 74 located near to the middle position of the *a*-axis. As in the case of the (1 0 0) twinning, the position of an adjacent oxygen atom at the height of 26 should be slightly adjusted to the height of 24 in Fig. 4a to make this relation exact. It is then possible to rotate the whole structure through this axis without altering the relative positions of neighbouring atoms. Fig. 4b shows a possible [1 0 0] twin structure built in this way, which is coincident with the [1 0 0] rotation twinning. It should be pointed out that the (1 0 0) twinning is formed by the operation of glide plane symmetry with a translation $b/2$. So these two twin may differ from each other in terms of structure because they are introduced by different symmetries.

3.2. Intergrowth of tetragonal and monoclinic structures

The tetragonal phase was also detected, although it is considered as a metastable phase at room temperature (its stability regime is within the range 1000–2000 °C). Fig. 5a shows an electron diffraction pattern from such a tetragonal grain with the electron beam along the [0 0 1] direction. There is a strong intergrowth between the two twin types of the monoclinic phase and the tetragonal phase. The electron diffraction pattern (Fig. 5b) shows the intergrowth of the tetragonal and the (1 0 0) twinned monoclinic phases . Two superimposed sets of reflections due to the tetragonal and monoclinic structures, respectively, illustrate the intimate intergrowth between them. Coincidence of the 2 0 0 reflection of the monoclinic structure with the 1 1 0 reflection of the tetragonal structure shows a completely coherent interface between them. From the definition of the reciprocal lattice vector, the [1 0 0]* and [0 0 1] vectors of the monoclinic lattice in reciprocal and real spaces are perpendicular to each other. It can be deduced that the [1 1 0] vector of the tetragonal structure, which is perpendicular to the [1 0 0]* reciprocal vector of the monoclinic structure, is parallel to the [0 0 1] vector of the monoclinic structure in Fig. 5b. As a result, the orientation relationship between the tetragonal and monoclinic phases determined directly from this pattern, is given as $[0\,1\,0]_m \| [0\,0\,1]_t$, $[0\,0\,1]_m \| [1\,1\,0]_t$ and $(1\,0\,0)_m \| (1\,1\,0)_t$, where subscripts m and t refer to the monoclinic and tetragonal zirconia, respectively.

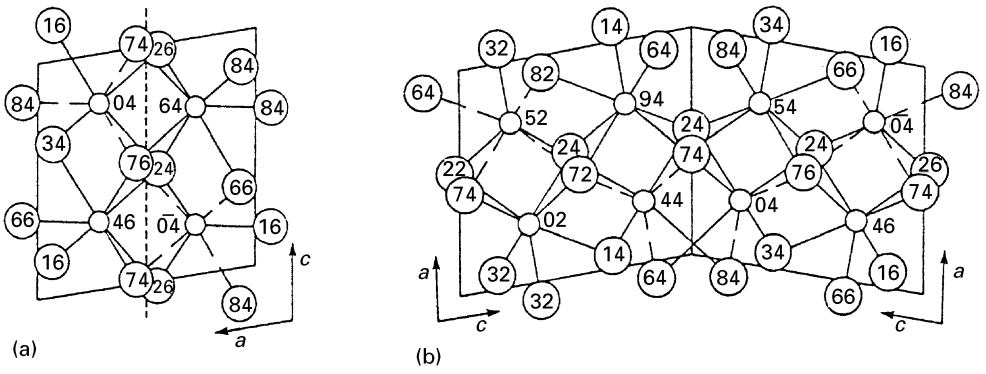

Figure 4 (a) Atomic arrangement of monoclinic ZrO_2 projected on the (0 1 0) plane. (– – –) The (1 0 0) twin plane, (○) oxygen and (○) zirconium. The heights of the atoms above the (0 1 0) plane are indicated by numbers, where the length of the *b*-axis is 1 0 0. (b) Suggested structural model for the [0 0 1] reflection twin; a very small adjustment of the oxygen atom at the interface was made.

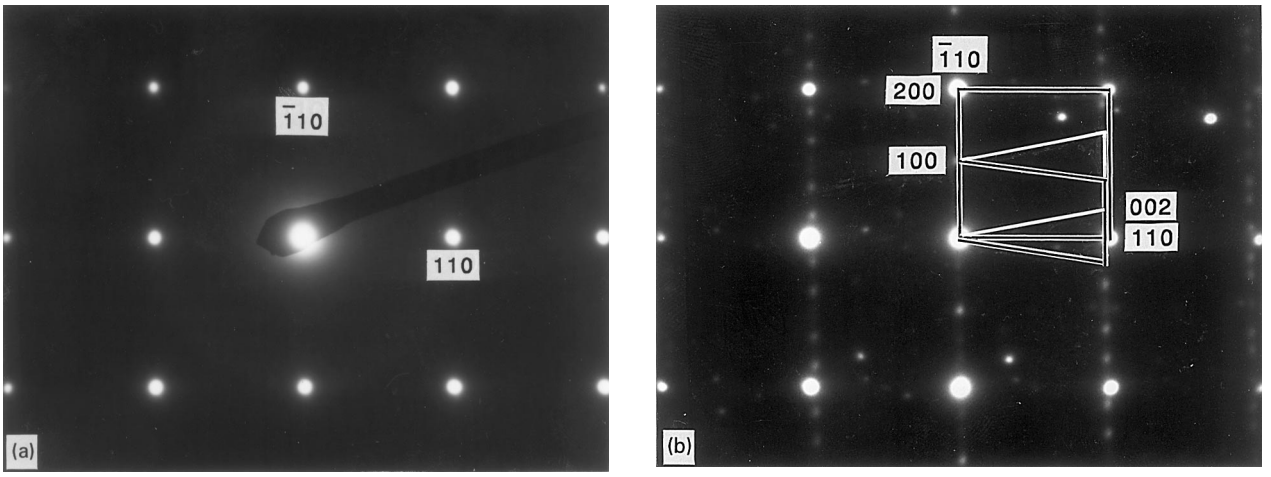

Figure 5 Electron diffraction patterns showing (a) the (0 0 1)* reciprocal plane of the tetragonal phase and (b) intergrowth with the (1 0 0) twinned monoclinic structure.

The one-dimensional superlattice with a double $\{1\,0\,0\}$ planar spacing resulting from the ordering of the yttrium cation in the lattice of tetragonal zirconia has been reported [16]. Fig. 6a and b show the electron diffraction patterns along the [0 0 1] zone axis of the tetragonal structure; intergrowth of the (1 0 0) and [1 0 0] twinned monoclinic and a two-dimensional superlattice with repeat periods of twice the *a* and *b* parameters of the fundamental lattice in real space, can be seen. The relative arrangement of the two phases in Fig. 6a is nearly the same as that in Fig. 5b, whereas in Fig. 6b, the 0 0 2 instead of the 2 0 0 reflection is coincident with the 1 1 0 tetragonal reflection, maintaining the complete coherency of the two structures, but changing their relative orientations. Therefore, an alternative orientation relationship can be derived from Fig. 6b as follows: $[0\,1\,0]_m \| [0\,0\,1]_t, [1\,0\,0]_m \| [1\,1\,0]_t$, $(0\,0\,1)_m \| (1\,1\,0)_t$. Fig. 7a shows the coexistence of the tetragonal and monoclinic phases accompanied by two kinds of twinning. Misorientation between the two couples of twin-related monoclinic lattices within the (0 1 0) plane is obvious. The misoriented angle is determined to be 9°15′. In this case, the (1 0 0) plane and [0 0 1] axis of the (1 0 0) twin variants are perpendicular to the (0 0 1) plane and the [1 0 0] axis of the [1 0 0] twin variants and parallel to the (1 1 0) plane and [1 1 0] direction of the tetragonal phase. Based upon these diffraction data, the relation between the tetragonal and monoclinic lattices during phase transformation can be suggested. The $\langle 1\,1\,0 \rangle$ vectors and the parallel $\{1\,1\,0\}$ planes of the tetragonal lattice became either the *a*- or *c*-axes and the $\{0\,0\,1\}$ or $\{1\,0\,0\}$ planes, respectively, or their twin-related axes and planes, of the monoclinic structure, and resulted in

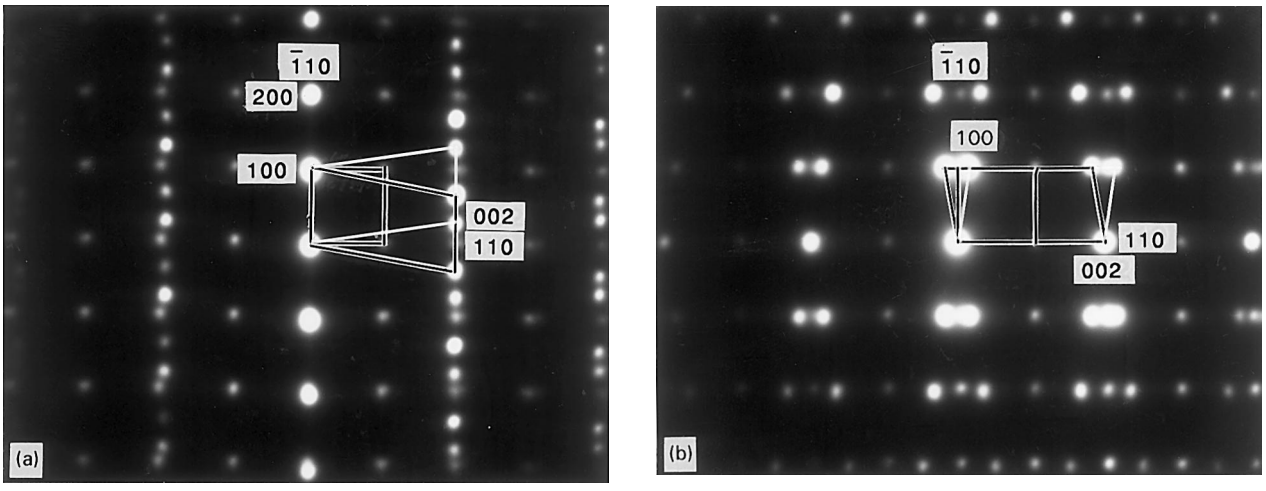

Figure 6 Electron diffraction patterns showing the coexistence of the superstructure of tetragonal phase and (a) (1 0 0) and (b) [1 0 0] twinning of monoclinic ZrO_2.

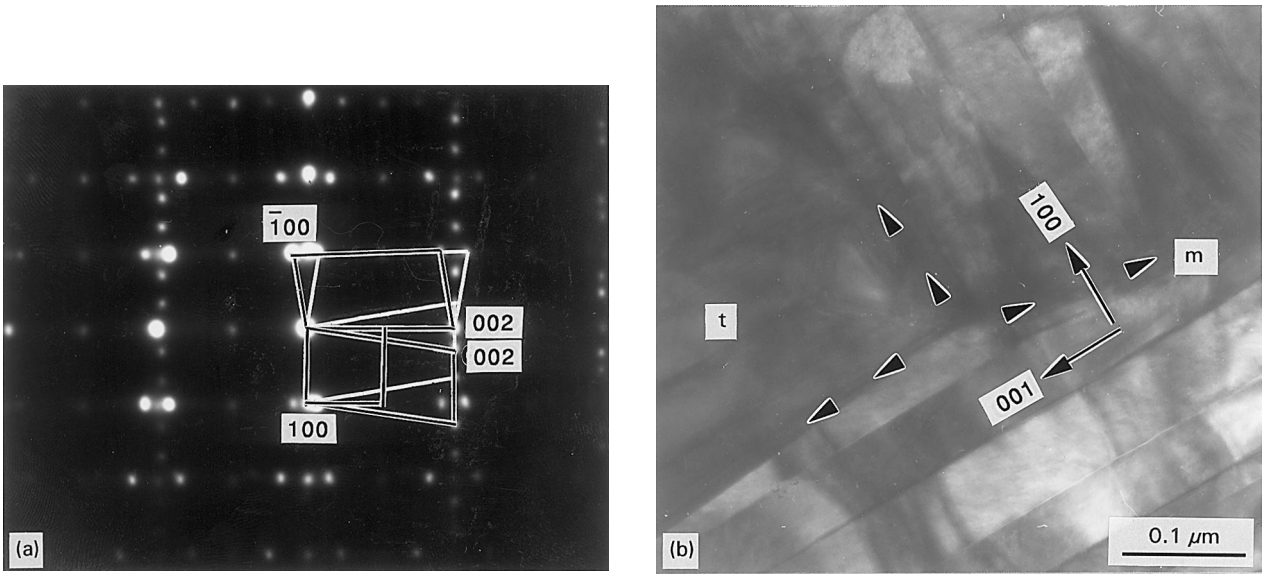

Figure 7 (a) Electron diffraction pattern with the incident beam parallel to the [0 0 1] zone axis of tetragonal ZrO_2 showing intergrowth of the superlattice of tetragonal phase and (1 0 0) and [1 0 0] twinned monoclinic ZrO_2; the two indicated matrix lattices as well as their twinned lattices are twisted through 9°15′ in the (0 1 0) plane. Such oriented lattices are also coincident with orientation variants. (b) The corresponding bright-field micrograph, exhibiting intergrowth of tetragonal and monoclinic grains with two kinds of the twinned bands. The average size of these bands is about 50 nm. m and t refer to monoclinic and tetragonal grains, respectively. (1 0 0) and [1 0 0] twinning is present at right top and bottom. The indicated grain boundary is approximately parallel to the (1 0 0) plane. Two interphase interfaces marked by arrow heads are coincident with $(1\,1\,0)_t \| (1\,0\,0)_m$ and $(1\,1\,0)_t \| (0\,0\,1)_m$ types. The band-like microstructure is also visible in tetragonal ZrO_2.

microstructure with highly oriented grains. For example, the $[1\,1\,0]_t$ vector and $(1\,1\,0)_t$ plane changed into the $[0\,0\,1]_m$ vector and $(2\,0\,0)_m$ plane in Figs 5b and 6a and into the $[1\,0\,0]_m$ vector and $(0\,0\,1)_m$ plane in Fig. 6b. Fig. 7a shows a combination of them. The corresponding bright-field image is shown in Fig. 7b, where the tetragonal and two monoclinic grains with multiple (1 0 0) and [0 0 1] twinned layers with an average size of about 50 nm, are intimately grown. The indicated interphase boundaries are coincident with the $(1\,1\,0)_t \| (1\,0\,0)_m$ and $(1\,1\,0)_t \| (0\,0\,1)_m$ types. From Fig. 4a it is known that the (1 0 0) and (0 0 1) planes are different from each other; therefore, it can be inferred that different interfacial structures will be introduced at the $\{1\,1\,0\}_t \| (1\,0\,0)_m$ and $\{1\,1\,0\}_t \| (0\,0\,1)_m$ boundaries, respectively. The indicated grain interface deviated slightly from the (1 0 0) plane in a range of 5°, about half of the misoriented angle (9°15′) of two grains. Such a deviated boundary may be favourable for reducing the misfit of atoms near the interface due to relaxation of the atom. The band-like character within the tetragonal phase can also be seen clearly, consisting of the (1 1 0) planar defects revealed in the corresponding high-resolution image (Fig. 8). Such a defect may result from the concentration of other cations such as yttrium on the (1 1 0) plane.

3.3. Orientation variants

As a consequence of phase transformation, a domain structure with different interfaces is introduced, i.e. intergrowth of the variants with distinct orientations. Fig. 9a is an electron diffraction pattern showing such two orientation variants, the (1 0 0) plane of one variant is parallel to the (0 0 1) plane of the other. Two variants are related by a rotation around the common *b*-axis through 180°-β (80°45′) or its complementary angle β (99°15′). Based upon the properties of real and reciprocal vectors, the orientation relationship of the two variants derived from this figure are as follows: $(0\,0\,1)_I \| (1\,0\,0)_{II}$, $[1\,0\,0]_I \| [0\,0\,1]_{II}$ and $[0\,1\,0]_I \| [0\,1\,0]_{II}$. The electron diffraction patterns (Fig. 9b–d) taken in the same direction show intergrowth of the orientation and twin variants. In these figures both the (1 0 0) and [1 0 0] twin variants are included, respectively. Two pairs of {1 0 0} and {0 0 1} planes arranged in parallel between the orientation and twin variants were produced. In addition to the relation in Fig. 9a, another orientation relationship of $(1\,0\,0)_I \| (0\,0\,1)_{II}$, $(0\,0\,1)_I \| (1\,0\,0)_{II}$ and $[0\,1\,0]_I \| [0\,1\,0]_{II}$ can be found in Fig. 9b and c. Two sets of such orientation are present in Fig. 9d. It should be pointed out that the two matrix lattices are not coincident with any of the twin-oriented lattices by rotating one of them through an angle around the incident electron beam, as occurs between two matrix lattices, i.e. there is not the same relation as that of the orientation variants between the matrix and two twinnings, although the orientation variants can also be considered as rotation twinning with the specific rotation angles around the common axis from the crystallographic point of view. The two twin variants in Fig. 9d also form the same orientation variants as the two matrix lattices. Consequently, the number of independent variants is only two.

Based upon the suggested lattice correspondence of the $\{1\,0\,0\}_m$ and $\{0\,0\,1\}_m$ parallel to the $\{1\,1\,0\}_t$ planes during tetragonal to monoclinic phase transformation, all possible arrangements of orientation variants can be deduced and are given in Table I. the misorientation angles between these variants are 80°45′, 9°15′ and 90°, respectively, i.e. a total of four orientation variants will be separated by three distinct interfaces. Generally, the arrangement of these orientation variants can be divided into two classes according to the relative orientation of the corresponding lattice planes and vectors, i.e. the parallel and perpendicular orientations. For the parallel orientation, the variants have both a pair of parallel lattice planes and a pair of parallel lattice vectors. In the perpendicular case, the variants have either two pairs of perpendicular planes or vectors. As an example, the differently oriented monoclinic lattices of matrix and of twinning in Fig. 7a are coincident with the orientation variants with a misorientation angle of 9°15′ and can be used to illustrate the perpendicular orientation.

The group theory has been used to study the orientation variants due to disorder–order transformation in many alloys and oxides [17, 18]. The total number of variants can be predicted by the order of the point group of the matrix phase divided by that of the product phase. For tetragonal zirconia, the point group is determined to be 4/*mmm*, and 2/*m* corresponds to monoclinic structure. Their orders are 16 and 4, respectively. So the number of orientation variants is predicted to be 16/4, i.e. four distinct variants could be introduced in the process of tetragonal to monoclinic phase transformation. When viewed along a lattice direction, the number of orientation variants is usually equal to the operation elements of lost symmetry of the matrix phase in the same direction during phase transition. For example, from the orientation relationship determined above, it is known that the [0 0 1] four-fold symmetry (four operation elements) of the tetragonal phase is reduced to two-fold symmetry (two operation elements) when

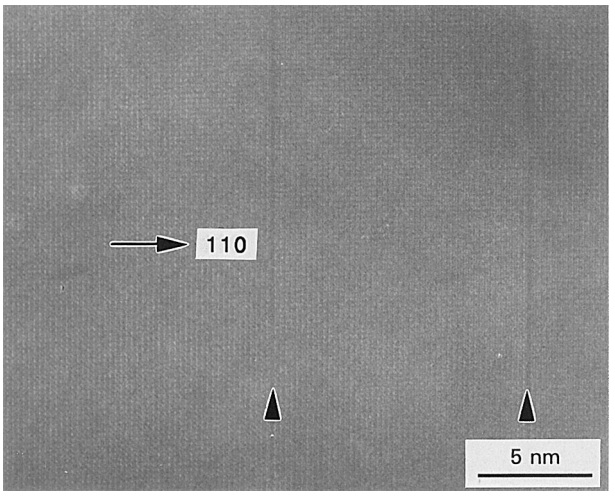

Figure 8 [0 0 1] high-resolution image demonstrating the (1 1 0) planar defect in tetragonal ZrO_2, as marked by arrow heads.

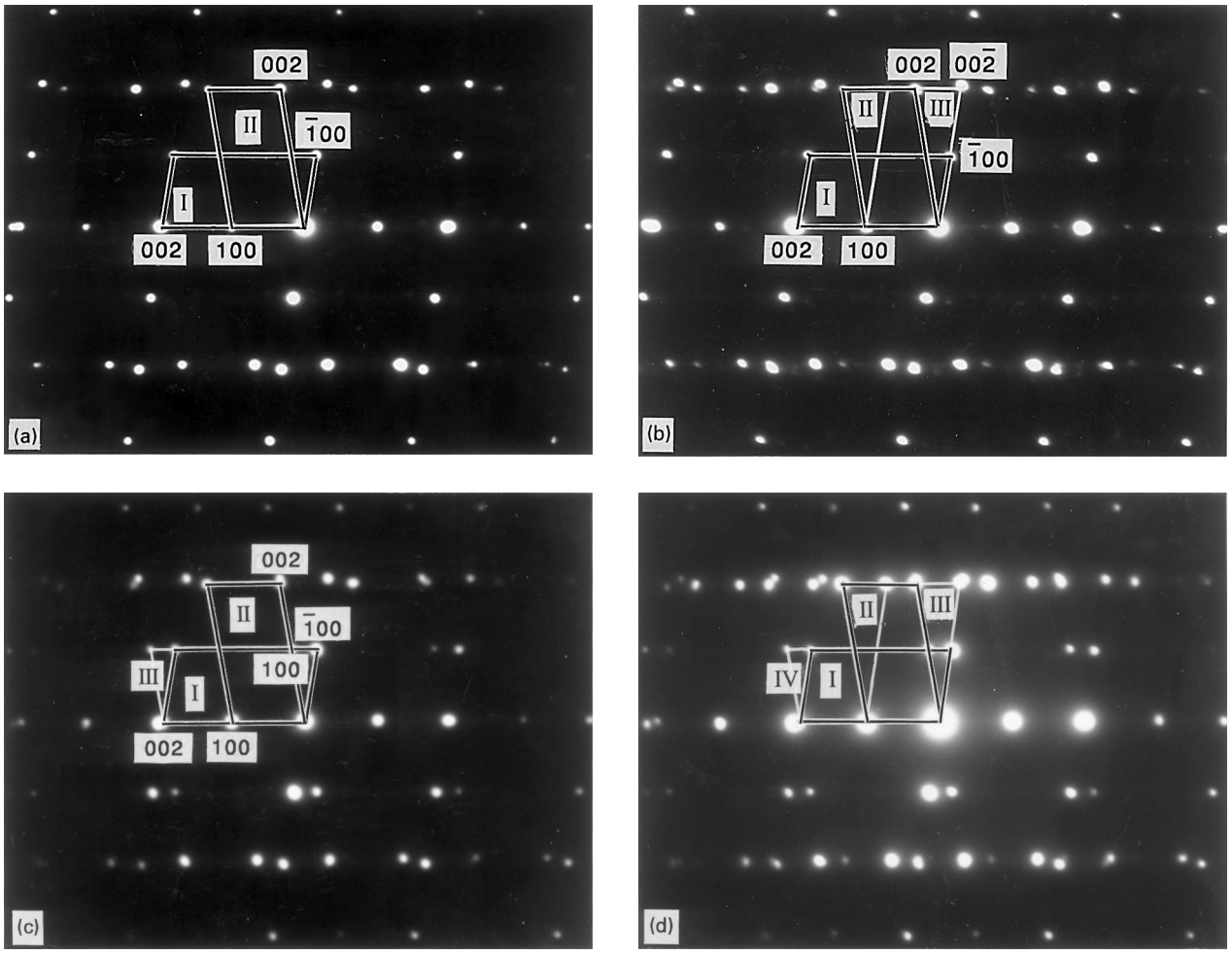

Figure 9 [0 1 0] electron diffraction patterns depicting (a) two orientation variants (I and II), (b) two orientation and a (1 0 0) twin variant (III), (c) two orientation and a [1 0 0] twin variant (III) and (d) two orientation and the (1 0 0) and [1 0 0] twin variants (III and IV); the orientation and twin variants are outlined with different lines.

TABLE I Possible arrangement of the orientation variants derived, based on the relation of the $\{1\,0\,0\}_m$ and $\{0\,0\,1\}_m$ parallel to the $\{1\,1\,0\}_t$ planes

Orientation relation	Misorientation	Observation	Frequency
$\{1\,0\,0\}_I \| \{0\,0\,1\}_{II}$, $\langle 0\,0\,1\rangle_I \| \langle 1\,0\,0\rangle_{II}$	80°45′	Yes	High
$\langle 1\,0\,0\rangle_I \perp \langle 0\,0\,1\rangle_{II}$, $\langle 0\,0\,1\rangle_I \perp \langle 1\,0\,0\rangle_{II}$ ($\{1\,0\,0\}_I \perp \{1\,0\,0\}_{II}$, $\{0\,0\,1\}_I \perp \{1\,0\,0\}_{II}$)[a]	9°15′	Yes	Low
$\langle 1\,0\,0\rangle_I \perp \langle 1\,0\,0\rangle_{II}$, $\langle 0\,0\,1\rangle_I \perp \langle 0\,0\,1\rangle_{II}$ ($\{1\,0\,0\}_I \perp \{1\,0\,0\}_{II}$, $\{0\,0\,1\}_I \perp \{0\,0\,1\}_{II}$)[a]	90°	No	–

[a] Equivalent orientation.

it is transformed to the monoclinic phase. Therefore, the orientation variants could be discovered and the total number is two. These two variants are related by the lost symetries, 4^1 or 4^3 operation, i.e. they are 90° orientation variants. There is an obvious contradiction between the observation and calculation due to the martensitic nature of the tetragonal to monoclinic phase transformation. Complicated variants were found in the present study. Variants with the perpendicular orientation have seldom been observed during examination. 90° orientation variants have not been determined in this preliminary study, although it is possible to introduce such variants during tetragonal to monoclinic transformation. Geometrically, the twin interfaces are perfect without misfit of atoms, the interface between variants with a pair of parallel planes may have a better fit of atoms near the interface than that with two pairs of perpendicular planes. These three kinds of interfaces correspond to different interfacial energies, their stabilities may also be different. The twin interfaces are most stable and frequently found. The stability and frequency of an interface with a pair of parallel planes are higher than that with two pairs of perpendicular planes, but less than the twin interfaces. The bright-field image (Fig. 10) illustrates a general view of such a domain structure. These orientation variants and the accompanied twinnings are highly oriented to form the matrix texture.

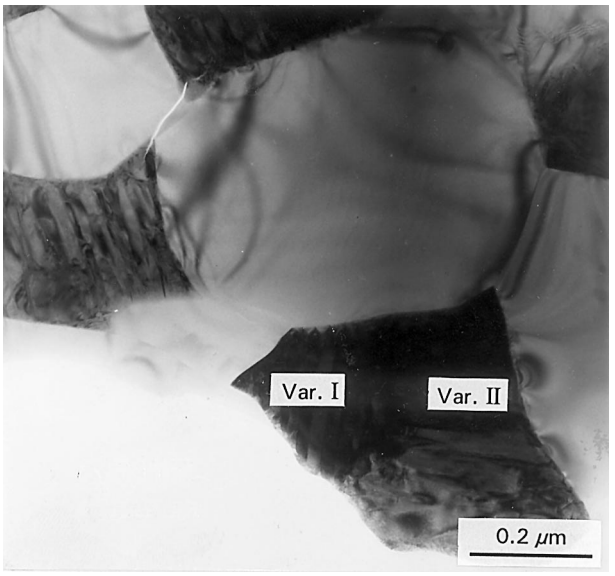

Figure 10 [0 1 0] bright-field image showing the orientation variants of monoclinic ZrO_2; multiple twinning is revealed in the marked grains.

4. Conclusion

The major features of the observed microstructure confirm the presence of highly ordered grains, which result in the formation of a matrix with texture characteristics. Such a microstructure is favourable for unifying the effects of fibre strengthening and fibre toughening. The improvement in the mechanical properties can be mainly ascribed to this homogenous microstructure. The sol–gel method shows a possibility of optimizing the dispersion of the fibres in the ceramic matrix and producing a well-developed matrix texture of fine grains, submicrometre, in size, which contributes mainly to the high fracture toughness of 9.7 MPa $m^{1/2}$ and a fracture strength of the order of 935–1110 MPa, and thus may be a competitive procedure for making reinforced ceramic composites. The information resulting from the TEM observations contributes to an increased understanding of the role of the microstructure on the mechanical response and thus, gives a basis for the design of advanced ceramic composites.

Acknowledgement

Y. G. Wang is grateful for a grant from Department for Scientific and Industrial Research, The Research Council of Norway.

References

1. R. M. McMEERING and A. G. EVANS, *J. Am. Ceram. Soc.* **65** (1982) 242.
2. B. BUNDIANSKY, J. W. HUTCHINSON and J. C. LAMBROPOULOS, *Int. J. Solid Struct.* **19** (1983) 337.
3. D. B. MARSHALL and M. V. SWAIN, *J. Am. Ceram. Soc.* **71** (1988) 399.
4. K. NIIHARA, N. ÜNAL, A. NAKAHIRA, *J. Mater. Sci.* **29** (1994) 164.
5. N. CLAUSSEN, *J. Am. Ceram. Soc.* **59** (1976) 49.
6. G. GRATHWOHL and T. LIU, *ibid.* **74** (1991) 318.
7. R. A. CUTLER, J. R. REYNOLDS and A. JONES, *ibid.* **75** (1992) 2173.
8. V. K. WADHAWAN, *Phase Transitions* **3** (1982) 3.
9. T. LOG, R. A. CUTLER, J. F. JUE and A. V. VIRKAR, *J. Mater. Sci.* **28** (1993) 4503.
10. J. F. JUE and A. V. VIRKAR, *J. Am. Ceram. Soc.* **73** (1990) 3650.
11. N. GLAUSSEN, K. -L. WEISSKOPF and M. RUEHLE, *ibid.* **69** (1986) 288.
12. J. HOMENY, W. VAUGHN and M. K. FERBER, *Am. Ceram. Soc. Bull.* **67** (1987) 333.
13. J. S. ZHANG, F. XIA, C. LUO, L. H. CAO, K. F. CHAO and W.P. HU, *Acta Metall. Sinica* **3B** (1990) 200.
14. G. TEUFER, *Acta Crystallogr.* **15** (1962) 1187.
15. J. D. McCULLOUGH and K. N. TRUEBLOOD, *ibid.* **12** (1959) 507.
16. Q. LI, L. C. WANG, J. G. ZHANG, J. M. ZHU, D. FENG, G. Y. MENG and Q. L. XU, in "Proceedings of the 5th Asia and Pacific Conference on Electron Microscopy", edited by K. H. Kuo and Z. H. Zhai, Vol. 1 (World Scientific, Singapore, 1992) p. 458.
17. G. VAN TENDLOO and S. AMELINKX, *Acta Crystallogr.* **A30** (1974) 431.
18. Y. G. WANG, H. Q. YE, K. H. KUO, X. J. FENG, G. L. LAO and S. Z. LONG, *J. Mater. Sci.* **26** (1991) 814.

Received 10 May 1994
and accepted 13 February 1996